Strain response and energy dissipation of floating saline ice under cyclic compressive stress

Mingdong Wei[1], Arttu Polojärvi[1], David M. Cole[2], Malith Prasanna[1]

[1]Aalto University, School of Engineering, Department of Mechanical Engineering, P.O. Box 14100, FI-00076 Aalto, Finland.

[2]ERDC-CRREL (Ret.), 72 Lyme Rd., Hanover, NH 03768, USA

Correspondence to: Arttu Polojärvi (arttu.polojarvi@aalto.fi)

Abstract. Understanding the mechanical behavior of sea ice is the basis of ice mechanics applications. Laboratory-scale work on saline ice has often involved dry, isothermal ice specimens due to the relative ease of testing. This approach does not address the fact that the natural sea ice is practically always floating in seawater and typically has a significant temperature gradient. To address this important issue, we have developed equipment and methods for conducting compressive loading experiments on floating laboratory-prepared saline ice specimens. The present effort describes these developments and presents the results of stress-controlled sinusoidal cyclic compression experiments. We conducted the experiments on dry, isothermal (-10℃) ice specimens and on floating ice specimens with a naturally occurring temperature gradient. The experiments involved ice salinities of 5 and 7 ppt, cyclic stress levels ranging from 0.04–0.12 MPa to 0.08–0.25 MPa and cyclic loading frequencies of 0.001 Hz to 1 Hz. The constitutive response and energy dissipation under cyclic loading were successfully analyzed using an existing physically based constitutive model for sea ice. The results highlight the importance of testing warm and floating ice specimens and demonstrate that the experimental method proposed in this study provides a convenient and practical approach to perform laboratory experiments on floating ice.

1 Introduction

Climate change has led to an increased interest in polar sea areas and on ice behavior, since accurate predictions on the evolution of the ice conditions are crucial for modeling the future climate. Warming climate has also resulted in a search for more efficient marine transit routes, production of offshore wind power, industrial operations related to extraction of hydrocarbons, and even tourism in the north (Gagne et al., 2015; Serreze and Stroeve, 2015; Kern et al., 2019). Structural loads due to sea ice make these activities challenging. In-depth understanding of the physical and mechanical properties of sea ice is required to develop tools for modeling future ice conditions, the related ice–ice and ice–wave interaction problems, and for the design of safe and sustainable offshore structures

29　(Dempsey, 2000; Feltham, 2008, Herman et al., 2019a,b; Lu et al., 2018a,b; Ranta et al., 2017, 2018a,b; Tuhkuri

30　and Polojärvi, 2018; Polojärvi et al., 2015; Voermans et al., 2019; Cheng et al., 2019; Li et al., 2015).

31　This paper studies the mechanical behavior of laboratory-prepared saline ice specimens under cyclic loading. This

32　type of loading occurs in wave–ice and some ice–ice and ice–structure interaction problems – all important in the

33　changing polar environment. For example, warming climate causes an increase in the amount of open water and

34　broken ice fields, which strengthens the impact of waves on sea ice. From the perspective of pure ice mechanics

35　and modeling of ice, the cyclic loading experiments yield information on the elastic and viscoelastic components

36　of strain and their dependence on the physical, or microstructural, characteristics of the ice. The cyclic loading

37　tests also give insight into the fatigue of ice (Haskell et al., 1996; Bond and Langhorne, 1997; Langhorne et al.,1998;

38　Mellor and Cole, 1981; Murdza et al., 2019; Schulson and Paul, 2009; Iliescu et al., 2017; Iliescu and Schulson,

39　2002).

40　Cyclic loading experiments on freshwater ice have been performed since the forties (Kartashkin, 1947; Mellor and

41　Cole, 1981) and on saline ice since the eighties (Tabata and Nohguchi, 1980; Cole, 1995; Cole and Durell, 1995;

42　Cole et al., 1998). Cole and Durell (1995) studied the effects of temperature (from -5 to -50℃), cyclic stress

43　amplitude (from 0.1 to 0.8 MPa) and loading frequency (from 10^{-3} to 1 Hz) on the response of laboratory-grown

44　saline ice; the ice response was revealed sensitive to variations in these factors. Cole et al. (1998) investigated the

45　response of columnar first-year sea ice to cyclic loading and found that the elastic, anelastic, and viscous strains

46　varied according to the relation between the loading and preferred c-axis directions of the specimens. More recently,

47　Heijkoop et al. (2018) conducted strain-controlled cyclic compression tests on sea ice to ascertain the variation of

48　storage and loss compliances versus frequency. All of this earlier work has been performed using isothermal, dry

49　specimens.

50　An often-overlooked issue in laboratory-scale experimentation is that most sea ice problems involve ice that is

51　floating on water. Floating ice commonly has a through-thickness temperature gradient, resulting in a through-

52　thickness gradient in its mechanical properties. The latter point is important to address in experimentation and

53　modeling. The temperature gradient is implicitly taken into account in in-situ experiments on floating ice

54　(Langhorne et al., 2015; Smith et al., 2015; Wongpan et al., 2018). The cost of in-situ experimental campaigns,

55　however, is high and the experiments often require specially designed loading devices (Vincent and Dempsey,

56　1999; Dempsey et al., 1999, 2018; Cole and Dempsey, 2004). Consequently, the relatively low costs and

57　convenience of laboratory-scale work motivate the development of viable methods for laboratory-scale

58　experiments on floating ice. Such experiments can be used, for example, for thorough validation of material models

59　aiming to account for the temperature gradient in ice.

60   In the study presented here, stress-controlled sinusoidal cyclic compression experiments were performed on

61   laboratory-grown, non-oriented columnar saline ice specimens floating on salt water and repeated on dry,

62   isothermal (-10°C) specimens. The dry experiments were conducted to validate the performance of our newly

63   developed testing apparatus and experimental methods under commonly used test conditions. Moreover, the results

64   provide a reference on the different mechanical behavior of floating ice from that of the ice under such conditions.

65   The varied parameters were the ice salinity, cyclic stress amplitude and mean stress level, and the frequency of

66   cyclic loading. The results are comprehensively analyzed and discussed, and are shown to compare favorably with

67   the predictions of an existing physically-based constitutive model (Cole,1995). Techniques and observations

68   yielding increased insight of the behavior of sea ice in its natural conditions are introduced; Insight on floating,

69   rather warm, ice is important, as future sea ice is expected to be on average warmer than now (Boe et al., 2009;

70   Blockley and Peterson, 2018; Ridley and Blockley, 2018).

71   The paper is organized as follows. Section 2 describes the specimen preparation, the experimental set-up, and the

72   matrix of experimental variables. Section 3 presents the results from the experiments. Section 4 addresses

73   constitutive modeling and Section 5 discusses our findings with references to earlier work and Section 6 gives our

74   conclusions.

75   **2 Laboratory experiments of saline ice under cyclic loading**

76   **2.1 Saline ice specimen preparation and characterization**

77   The ice was grown in the cold room of Department of Mechanical Engineering, Aalto University using a tank

78   having dimensions of 1.15 m × 1.15 m × 0.98 m (width × length × depth) and meltwater salinities of 24 and 34

79   ppt. Rigid foam insulation was placed on the sides and bottom of the tank and heating cables were placed around

80   the bottom perimeter to inhibit freezing from the structural members of the tank. Additionally, a hose for draining

81   excess water was installed near the base of the tank, to prevent the accumulation of water pressure under the ice

82   sheet during its growth. Such pressure could cause microcracking of ice or generate additional loads on the tank.

83   Specimens having the nominal dimensions of 0.60 m × 0.30 m × 0.10 m were prepared by placing high-density

84   polyethylene molds into the tank before seeding (Figure 1). The tolerance of the specimen dimensions was ±2 mm

85   (in all stress calculations below, the measured dimensions of the specimens were used). The molds floated with

86   2–3 mm of freeboard. Next, the saline water was chilled to about -1.5°C, the cold room temperature dropped to ≈

87   -20°C and the tank was seeded by spraying very fine mist of fresh water over the tank as is typically done to seed

88   ice sheets in larger-scale test basins (Gow, 1984; Li and Riska, 1996).

89   After the seeding, the room temperature was increased to -14°C for three days and then -10°C for two days to

90   produce the desired specimen thickness of 10 cm. The ice sheets made using 24 ppt and 34 ppt-saline water reached

91   average salinities of 5 and 7 ppt, respectively, and their densities were 886 ± 19 and 879 ± 16 kg·m^{-3}, respectively.

92   The specimens used in the dry experiments (Figure 2a and 3) were sealed in plastic bags and stored in a freezer at

93   -10°C for 1–2 days before testing. However, for the floating ice experiments (see Figure 2b), the specimens were

94   ejected from the molds, placed in plastic bags with water from the growth tank and quickly transferred to the test

95   basin to minimize brine drainage during the transfer.

96   Before the experiments, the columnar microstructure of the ice was verified by producing and inspecting thin

97   sections as detailed by Langway (1958). Of special interest was the microstructure close to the specimen

98   boundaries since such molds are somewhat uncommon in ice specimen preparation. Figure 4 shows two typical

99   thin sections from near the boundary of a specimen produced using 24-ppt-saline water; one is for the vertical and

100   the other for the horizontal direction as indicated. Figure 4a shows the columnar structure of the ice. The horizontal

101   view in Figure 4b provides a way to estimate the average grain size by dividing the section area by the number of

102   grains; the average grain size was ≈ 3.5 mm. The Schmidt equal area net pole projection for one of the thin sections

103   shown in Figure 5 confirms that the c-axes were unaligned in the horizontal plane, as intended.

104

105   **2.2 Equipment, test matrix and experimental procedure**

106   The experiments were conducted in the same cold chamber used for the saline ice production. As Figures 2 and 3

107   illustrate, an externally mounted electrohydraulic cylinder applied loads to the specimens. The piston passed

108   through a sealed port in the side of the test tank. The piston had a maximum stroke of 800 mm and a loading

109   capacity of 100 kN for compression and 60 kN for tension. The load cell had an accuracy of $\pm$ 5 N, which is

110   sufficient for all stress levels and cycles of the experiments here. The test basin was constructed of waterproof

111   plywood. The system employed a camera for remote monitoring of the experiments, a three-channel temperature

112   datalogger to record the temperature profile of floating ice during testing, a Data Acquisition Processor (DAP)

113   board (model: Data Translation DT9834), and fixtures for arranging displacement sensors to the ice specimens.

114   The temperature datalogger had a maximum sampling rate of one datum per five seconds, its measurement range

115   was from -100 to 1300°C, and an accuracy of $\pm$ 0.5°C. The DAP board could achieve a maximum scan rate of

116   500,000 samples per second.

117   The loading system has a self-equilibrating geometry in that the compressive force applied by the electrohydraulic

118   piston and transmitted through the specimen is balanced by a tensile force in the external load frame (Figure 3).

119   Care was taken to center the loading piston and the reaction plates on the vertical dimension of the load frame.

The ice deformation was measured as follows. Before the test, two holes were drilled on the specimen. Two iron rods with the cross-section of 5 mm × 5 mm were then inserted into the holes and frozen in place using a small quantity of cold fresh water. The relative displacement of the rods was monitored by two linear variable differential transformer transducers (LVDTs, model: HBM WA2, with a measurement range and accuracy of 2 and ± 0.001 mm, respectively). This relative displacement was used to determine the strain response of the specimen. As shown in Figures 2 and 3, the LVDTs were mounted on a rectangular steel placed across the basin.

The air temperature was kept at -10°C during all testing. To measure the through-thickness temperature gradient in all of the floating ice experiments, temperature probes were frozen into three 2.5 mm-diameter, 50 mm deep holes were drilled on one side face of the specimen. As shown in a sketch of Figure 6a, one measurement point was in the middle of the specimen from the vertical direction, and the other two were 1.5 mm away from the upper and lower surfaces of the specimen, respectively. During each floating ice experiment, temperature readings from all three channels remained constant for the duration of the experiment, indicating that the thermal gradient was unaffected by the cyclic loading.

Figure 6b presents typical temperature profiles measured in two floating ice specimens. For the 5-ppt-saline floating ice, the temperature near the top surface, in the middle and near the bottom surface of the specimen was measured to be -3.0, -2.3 and -2.2°C, respectively, while the values were -3.1, -2.4 and -2.1°C, respectively, for the 7-ppt-saline ice floe. These temperature readings suggest that the average temperature of the floating ice was -2.5°C, much higher than the air temperature of the cold chamber (-10°C). The water temperature at five centimeters below the water surface was measured to be ≈ -1.8°C in the floating ice tests.

The test matrix called for applying relatively low cyclic compressive stress levels with the system in load control. Figure 7 presents the loading waveforms used in the experiments and the test matrix is given in Table 1. In the experiments, the ice was first loaded with a linear ramp to reach an initial compressive stress level, at which point a compressive haversine waveform was immediately applied. In Figure 7a, σ_{max} and σ_{min} represent the upper and the lower bounds of the cyclic compressive stress, respectively, and T denotes the period for one loading cycle. As indicated by Table 1, six periods ranging from 1 to 10^3 s were employed; these periods cover the main range of ocean wave periods, which usually vary from several seconds to tens of seconds (Reistad et al., 2011; Zijlema et al., 2012). In each dry test, only a fixed frequency was applied. Once the test was completed, the specimen recovered for 15 minutes before subsequent load cycles were applied. For all dry tests, the duration of the initial loading ramp was fixed to be 1 s. In each of the tests corresponding to $T = 1, 5, 10$ and 100 s, 18 cycles were applied ($N = 18$), while for those with $T = 500$ and 1000 s, $N = 9$ and 4, respectively. The sequence of loading cycles was in ascending order of T in all cases. As a time-saving measure, and to avoid freezing of the open water

151 in the basin, cyclic stresses with increasing periods were applied continuously in the floating ice tests. The number

152 of cycles for each period was as follows: $T = 1$, 5 or 10 s, $N = 10$, for $T = 100$ s, $N = 2$, and for $T = 500$ or 1000 s,

153 $N = 1$.

154 The cyclic compressive stress applied to the dry specimens varied from 0.08 to 0.25 MPa, which could be

155 justifiably expected to not lead to severe damage of the specimen while being high enough to generate measurable

156 strain (Cole and Dempsey, 2001). The stress in the floating experiments was lower, varying from 0.04 to 0.12 MPa,

157 to avoid damage. For each case listed in Table 1, two specimens harvested from two ice sheets were subjected to

158 each set of conditions. The specimens were named according to their salinity, test conditions (dry/floating), and

159 the ice sheet from which it originated. For example, specimen name Dry-5ppt-1 indicates that it came from the

160 first 5-ppt-saline ice sheet and was tested under the dry, isothermal conditions.

161 Figure 7b illustrates how the energy dissipation in the cyclic loading experiments was calculated. For common

162 engineering materials subjected to uniaxial cyclic compression, the strain along the compressive direction versus

163 the stress is usually characterized by hysteresis loops. The strain energy density dissipated in a loading cycle can

164 be determined by integrating the stress-strain curve. As shown in Figure 7b, the area under the loading curve

165 (region ABCF) represents the maximum strain energy input via the testing machine during a load cycle, and the

166 area under region CDEF denotes the strain energy released during the unloading portion of the cycle. The energy

167 density dissipation (EDD) in one full loading-unloading cycle is given by the difference between the areas of

168 regions ABCF and CDEF (Liu et al., 2017, 2018). The energy density consumed in the hysteresis loop can, in

169 general, be attributed to the internal friction and, in some cases, damage to the material. For each cycle, the energy

170 dissipation rate (EDR) can be defined as the ratio of the dissipated energy to the input energy, namely the area of

171 the region ABCDE divided by that of the region ABCF.

172 **3 Experimental results**

173 Figure 8 presents strain-time plots obtained from the dry experiments using specimen Dry-5ppt-1 under the

174 indicated conditions. The strain-time curves manifest the following feature: If a line would be drawn through the

175 maximum value for each cycle, the slope of the line would first decrease from its initial value for some number of

176 cycles and then settle down to an almost constant value. This observation means that the strain response of the ice

177 specimen under sinusoidal compressive stress reaches a relatively steady stage after the initial transient of the

178 anelastic strain is exhausted, and that in this steady stage the accumulated viscous or permanent strain increases

179 linearly with time. In addition, Figure 8 shows that the longer the period T of cyclic loading, the larger the strain

180 amplitude in one steady-stage cycle. The total amount of strain does not strictly increase with the loading period.

181 This may be because the loading platen and the specimen did not always achieve perfect contact immediately,

182 causing some error in the strain measured in this initial stage of loading. Once intimate contact was achieved, the

183 measured strain became reliable.

184 Figure 9 shows the stress-strain curves for the same experiments. In each case, the area of the hysteresis loop for

185 the first few cycles was comparatively large, and then gradually decreased to a constant value as the specimen

186 reached the steady deformation stage described in the previous paragraph. For example, the hysteresis loops after

187 the first stress cycle in the dry experiment with $T = 1000$ s are similar; $N = 4$ is enough for the dry specimen at T

188 $= 1000$ s to show steady-state response. Thus, the EDD (Figure 7b) decreases from its initial value to an

189 approximately constant value. It is clear that the steady-state hysteresis loop area increase with the period of the

190 cyclic loading, consistent with earlier studies (Cole, 1990; Murdza et al., 2018; Weber and Nixon, 1996).

191 Figures 10 and 11 display a set of strain-time plots and the corresponding stress-strain curves for the floating ice

192 experiments on the 5-ppt-saline ice specimens, respectively. The curves in these two figures show similar features

193 to those in Figures 8 and 9 for dry experiments: The floating ice also reached a steady state of deformation after

194 some loading cycles and the amplitude of the steady-state strain response still increased with T. Similar to the

195 results of the dry experiments, Figure 11 indicates that the longer the loading period, the larger the strain increment

196 of the floating specimen under one steady-state loading-unloading cycle. Comparison of Figures 9 and 11 in the

197 steady state shows that, for constant T, both the strain increment per cycle and the area of one hysteresis loop, are

198 larger in the floating ice experiments than in the dry experiments even though the stress levels are lower than in

199 the dry experiments. It is thus evident that the decreased stress levels in the floating ice experiments did not fully

200 compensate for the temperature effects on the viscous and viscoelastic components of strain as, for example, the

201 viscous strain rate of floating 5-ppt-saline ice specimen is fourteen times that of the corresponding dry specimen.

202 The energy density dissipation (EDD) and the energy dissipation rate (EDR) per cycle during steady-stage

203 deformation (Section 2.2 and Figure 7b) allow quantitative comparisons of the inelastic behavior of specimens as

204 a function of test conditions. These are presented in Tables 2 and 3 for all, except the 1-second-period, experiments,

205 for which the hysteresis loop areas are too small for accurate measurements. Tables 2 and 3 indicate that both the

206 EDD and the EDR decrease with the increase of loading frequency. Moreover, under the same frequency, the 7-

207 ppt-saline ice has larger EDD and EDR values than the 5-ppt-saline ice irrespective of the experiment type. In

208 addition, the floating ice experiments always exhibit higher EDD and EDR values than the dry experiments

209 regardless of the ice salinities. The differences in the values of EDD are especially significant for low frequencies.

210 For example, in the experiments with $T = 1000$ s, the average value of EDD for the 5-ppt-saline dry specimens is

211 only 24% of that of the 5-ppt-saline floating specimens and 44% of that of the 7-ppt-saline dry specimens. However,

212 for the experiments with $T = 5$ s, the average value of EDD in the former case is 47% and 77% of that in the latter

213 two cases, respectively. Thus, the ice salinity and the test conditions have a more significant influence on the

214 energy dissipation of the ice when the cyclic loading period is long.

215 **4 Material modeling**

216 The hysteresis loops of the stress-strain curves manifest viscous and anelastic properties of the ice. According to

217 previous studies (Cole, 1995; Leclair et al., 1999), in low-stress cyclic loading experiments, the microstructure of

218 the ice remains unaffected by loading, or in other words, no damage occurs within the material. In the present case

219 of polycrystalline ice, the anelastic deformation is mainly attributed to two relaxation mechanisms, lattice

220 dislocation relaxation and grain-boundary sliding. Viscous straining is attributable to basal dislocation glide. In

221 this section, a dislocation-based model (Cole, 1995; Cole and Durell, 2001), which accounts for these mechanisms,

222 is used to predict the strain response of the ice specimens based on their physical properties and experimental

223 conditions. Here the model is only briefly described, but a detailed description can be found from Cole et al. (1998),

224 where the model is also demonstrated to reproduce the viscous and anelastic behavior of dry specimens. Here the

225 applicability of the model in predicting the behavior of floating laboratory-prepared ice specimens subjected to

226 cyclic loading is tested for the first time.

227

228 **4.1 Brief description of the model**

229 In the physically based model by Cole (1995) and Cole and Durell (2001), the axial strain, ε, of ice under uniaxial

230 cyclic compression is considered to be composed of elastic, anelastic (delayed elastic) and viscous components,

231 denoted here as ε_e, ε_a and ε_v, respectively. The axial strain is expressed as

232 $$\varepsilon = \varepsilon_e + \varepsilon_a + \varepsilon_v .$$ (1)

233 In the case of sinusoidal stress waveform, ε_e can be written as

234 $$\varepsilon_e = \frac{\sigma(\omega, t)}{E_0},$$ (2)

235 where ω is the angular frequency of the stress waveform and E_0 is the unrelaxed modulus. Although detailed

236 expressions have been developed for the effective elastic modulus as a function of crystallography, brine and gas

237 porosity, and temperature, a simplified approach is adopted in the present effort. The anelastic component ε_a

238 incorporates both above-mentioned relaxation mechanisms to represent the time-dependent recoverable

deformation. For the steady-stage deformation, ε_a of ice subjected to sinusoidal compressive stress can be decomposed as (Cole and Dempsey 2001)

$$\varepsilon_a = \sigma(\omega,t)\left[D_1^d(\omega) + D_2^d(\omega) + D_1^{gb}(\omega) + D_2^{gb}(\omega) \right],\qquad(3)$$

where the compliance terms, D, with the superscripts "d" and "gb" denote the compliances induced by dislocation and grain boundary sliding, respectively. The compliance terms are defined as (Cole et al., 1998)

$$D_1^d(\omega) = \delta D^d \left\{ 1 - \frac{2}{\pi} \tan^{-1}\left[e^{\left(\alpha^d s^d\right)} \right] \right\}\qquad(4)$$

$$D_1^{gb}(\omega) = \delta D^{gb} \left\{ 1 - \frac{2}{\pi} \tan^{-1}\left[e^{\left(\alpha^{gb} s^{gb}\right)} \right] \right\}\qquad(5)$$

$$D_2^d(\omega) = \alpha^d \cdot \delta D^d \frac{1}{e^{\left(\alpha^d s^d\right)} + e^{\left(-\alpha^d s^d\right)}}\qquad(6)$$

$$D_2^{gb}(\omega) = \alpha^{gb} \cdot \delta D^{gb} \frac{1}{e^{\left(\alpha^{gb} s^{gb}\right)} + e^{\left(-\alpha^{gb} s^{gb}\right)}},\qquad(7)$$

where $S^d = \ln(\tau^d \omega)$; τ^d is the central relaxation time (Cole and Durell, 1995). α is a so-called peak broadening term, which accounts for the effect of a distribution in relaxation times of the basal plane dislocations. The grain boundary relaxation is calculated using similar mathematic expressions as the dislocation relaxation, but has a different strength, activation energy and peak-broadening term. The activation energy is 1.32 eV for the grain boundary relaxation and 0.55 eV for the dislocation relaxation (Cole and Dempsey, 2001). The peak-broadening terms for lattice dislocation relaxation and grain-boundary sliding relaxation are typically $\approx$ 0.5 and 0.6, respectively, determined experimentally by Cole (1995), Cole and Dempsey (2001) and also validated by Heijkoop et al. (2018). The strength of the dislocation relaxation is calculated from

$$\delta D^d = \frac{\rho \Omega b^2}{K},\qquad(8)$$

where b represents Burgers vector ($b = 4.52 \times 10^{-10}$ m); ρ denotes the mobile dislocation density, often found to be on the order of 10^9 m^{-2}; Ω is an orientation factor, determining the average basal plane shear stress induced by the background normal stress ($\Omega = 1/\pi \approx 0.32$ for a horizontal specimen made of unaligned columnar ice (Cole, 1995)); K is a restoring stress constant, determined as 0.07 kPa for polycrystalline ice in experiments (Cole and Durell 2001).

In Eq. (1), the viscous strain ε_v is often estimated with the following formulae (Cole and Durell, 2001):

$$\varepsilon_v = \int_0^t \dot{\varepsilon}_v d\bar{t}\qquad(9)$$

264
$$\dot{\varepsilon}_{\mathrm{v}} = \frac{\beta\rho\Omega^{1.5}b^2\sigma_{\mathrm{creep}}}{B_0}e^{\left(-\frac{Q_{\mathrm{glide}}}{kT^*}\right)},$$
(10)

265 where $\beta = 0.3$, $Q_{\mathrm{glide}} = 0.55$ eV, and $B_0 = 1.205 \times 10^{-9}$ Pa·s. k is Boltzmann's constant, T^* is the temperature in

266 Kelvins. By using the above definitions and equations, the strain of the ice specimen can be finally determined via

267 Eq. (1).

268

269 **4.2 Modeling**

270 In this study, the key quantity to be determined from the experiments is the dislocation density (ρ). With knowledge

271 of the microstructure and orientation factor (Ω), and given the experimental conditions, the anelastic term δD^{d} and

272 the viscous strain rate can be calculated directly. We opt here to determine E_0 empirically. These were done by

273 trial and error until the stress-strain curves generated by the model matched with those measured in the experiments

274 with $T = 10$, 100 and 500 s. By making the slopes of the modeled and experimental hysteresis loops for $T = 10$ s

275 comparable, E_0 could be determined. This is because the behavior of the specimens is mainly dominated by the

276 un-relaxed modulus E_0 when the loading frequency is high (here 0.1 Hz to 1 Hz), as indicated in Figures 9 and 11.

277 From Eqs. (9) and (10), one can find that the strain increment under one loading cycle is dependent on the

278 dislocation density ρ; based on this, the dislocation density ρ was estimated by using the experimental results of

279 $T = 100$ and 500 s and δD^{d} was then determined from Eq. (8). δD^{gb} was determined by referring to previous work

280 (Cole 1995) because the grain boundary relaxation strength could be reasonably assumed constant for the ice

281 material of interest here, and its effect on inelastic behavior of ice was significantly less than the dislocation

282 mechanism. The values determined for the parameters are tabulated in Table 4. Subsequently, the model based on

283 these parameter values was applied to predict the test results for other loading periods. An example of the

284 comparison of experimental and modeling results is presented in Figure 12, in which the steady-state strain curves

285 from all dry experiments on the 5-ppt-saline ice specimen are accompanied by the simulated ones.

286 Figure 12 shows that the modeled strain records compare well with those from the experiments with period $T = 1$,

287 5 and 1000 s. The model reproduced the steady-state strain response of the specimens very well for all tested

288 frequencies. Figure 13 presents the stress-strain hysteresis loops from the same experiments together with those

289 produced by the model. The hysteresis loops generated by using the model are very similar to those from the

290 experiments. The loop area increases with T in both the experiments and simulations.

291 For assessing the model in more detail, the values of EDD and EDR derived using it are given in Tables 5 and 6,

292 respectively, and moreover, compared with the data from all the experiments (the test matrix is given in Table 1).

293 Tables 5 and 6 indicate that the model predicts well the values of EDD and EDR for all cyclic loading periods

294 studied here. In general, the error in the predicted EDD and EDR values are within 20%, with the exception of

295 only few cases. No obvious trend between the magnitude of error and loading period or experiment type was

296 observed. Note that for a given ice specimen, one dislocation density value adequately models the steady-state

297 strain responses and energy dissipation values in tests conducted with different frequencies. The value of

298
299 dislocation density, thus, remained constant through the cyclic loading.

300 **4.3 Further validation**

301 The above results show that the model can yield satisfactory predictions on the viscous and anelastic behavior of

302 both dry and floating specimens. One may argue that the good agreement between the model predictions and the

303 experimental results only indicates the capability of the model to predict the results for the experiments with the

304 same stress levels as those used to calibrate the model parameters. To check whether the model can predict the

305 results of the experiments with different stress levels than those above, additional experiments were performed on

306 specimen Dry-5ppt-1 with higher stress (0.1–0.3 MPa) and on specimen Floating-7ppt-1 with lower stress (0.005–

307 0.085 MPa) (Nominal cyclic stress of 0.005–0.085 MPa is low, but the setup could achieve it: With the accuracy

308 of the system, the actual stress applied to the specimen was 0.005 (±0.001)–0.085 (±0.003) MPa). The model was

309 then used to determine the strain response and energy dissipation in these tests using the parameterization based

310 on the experiments of Section 3 (Table 4).

311 Figure 14 compares the stress-strain hysteresis loops obtained in the supplementary experiments with the

312 predictions yielded from the model. Good agreement is observed between the predicted and measured hysteresis

313 loops. Again, the relative errors in the EDD and EDR values are found to be less than 20% for most data sets. The

314 model is, indeed, capable of predicting the deformation of saline ice in a dry environment or when floating in water

315 irrespective of the stress level (given that the stress levels are moderate and do not cause an increase in dislocation

316 density during deformation). The applicability of the model is highlighted by the fact that once the model

317 parameters are calibrated through benchmark experiments (the elastic modulus and dislocation density in the

318 present case), it yields sound predictions for the experiments conducted with other stress levels.

319 **5 Discussion**

320 Although past laboratory-scale work has provided insight into the mechanical behavior of sea ice, the work has

321 been mostly performed using relatively cold, dry and isothermal specimens. The results above indicate that more

322 attention should be paid to the mechanical behavior of relatively warm, floating ice with a naturally occurring

323 temperature gradient. Here efforts were made to develop a relatively low-cost, convenient and useful approach for

324 laboratory-scale floating ice experiments and for preparing small-scale, saline columnar ice specimens. The thin

325 sections (Figures 4 and 5) indicated that the measures taken on the ice production guaranteed the generation of

326 non-oriented columnar ice. Moreover, the thin sections showed that the molds used for specimen preparation do

327 not influence the columnar ice microstructure. This is encouraging, as molds are not often incorporated into

328 growing sheets of non-oriented columnar ice. The use of molds in this way significantly simplified specimen

329 preparation and resulted in accurate dimensions. The molds are especially effective in the experiments on floating

330 ice specimens: The specimens thus produced have proper dimensions, require no cutting, have a realistic

331 temperature gradient and can be quickly transferred to the test basin, so brine loss is minimized.

332 The results above are in qualitative agreement with what would be expected for floating ice, as for example,

333 floating specimens having through thickness thermal gradient and mean temperature of -2.5°C exhibit lower

334 modulus and more pronounced inelastic deformation in comparison with dry specimens at -10°C, as would be

335 expected based on full-scale observations on the effect of temperature on this property (Timco and Weeks 2010;

336 Cole 2020). This gives confidence on the methods employed in the production and mechanical testing of the

337 specimens. Further, the good agreement between the results for floating ice and the corresponding model

338 predictions show quantitative validity of the approach taken here. All-in-all, the results suggest that the chosen

339 experimental techniques (including the loading system, the strain measurement scheme, the data acquisition

340 system and settings) worked well and provided useful results for the analysis. An exception is some of the 1-

341 second-period experiments, which yielded strain responses with unexpected features; this is because the hysteresis

342 loop areas are very small in size, making accurate measurements with the used set-up challenging. This could be

343 circumvented in the future experiments by using techniques and devices with even higher precision and setting a

344 higher sampling rate of data acquisition. The methods proposed in this study to conduct laboratory experiments

345 on floating ice experiments are practical and can provide a convenient approach for relatively low-cost

346 experimentation on floating ice.

347 The laboratory work here not only demonstrated the availability of the proposed experimental methods, but also

348 contributes to the understanding of the constitutive behavior of ice. A common trend in developing material models

349 is to ensure they have a solid physical basis, that is, that they are based on an understanding of the physical

350 processes that underlie the mechanical phenomena of interest. Above we used one such physically-based model

351 introduced by Cole (1995). Earlier work, which has been based on the experiments resembling the dry experiments

352 here, has shown that the model is capable of predicting the inelastic deformation of sea ice via dislocation-based

353 mechanisms and is able to estimate the effective dislocation density in ice from experimental results. Here the

354 model was successfully validated against the results from the floating ice experiments. Moreover, the results

355 indicated that once the constant dislocation density value of the specimens was determined, the model adequately

356 predicted the steady-stage deformation for the cyclic loading experiments conducted with different frequencies

357 and stress levels. Even if the use of floating specimens could be considered to only address the temperature profiles

358 of in-situ floating ice (with some other environmental conditions of natural ice floes ignored), the above results

359 bring confidence to the model and demonstrate its potential in modeling practical applications involving ice in

360 such conditions, especially considering that some research has been launched to devote to a numerical

361 implementation of the model (O'Connor et al., 2020).

362 The good agreement between the experimental and modeling results also motivates discussion on the parameter

363 values in Table 4. Expectedly, the floating ice specimens have lower unrelaxed moduli than the dry specimen. For

364 the 5-ppt and 7-ppt-saline ice, the average elastic modulus of the floating specimens is 66% and 55% lower than

365 that of the dry specimens, respectively. In the dry experiments, the isothermal 7-ppt-saline ice has a 31% lower

366 average elastic modulus than the 5-ppt-saline ice. In the floating ice experiments, the 7-ppt-saline specimen still

367 has a lower average elastic modulus than the 5-ppt-saline specimen, but the difference, 8%, is not as prominent as

368 in the dry experiments. Thus, the fact that the floating ice had a realistic temperature profile had a larger influence

369 on the elastic modulus of ice than the variation of the ice salinities studied here.

370 Table 4 also indicates that the dislocation densities determined for the ice specimens were on the order of $\sim10^8$–

371 10^{10} m^{-2}, and thus were in good agreement with values in the 10^9 m^{-2} order of magnitude given by Cole (1995).

372 Moreover, the dislocation density of the floating ice was approximately one order of magnitude greater than that

373 of the dry specimen. Note that there is precedent showing the dislocation density of ice increasing with temperature

374 (Cole and Durell, 2001; Cole, 2020). The same trend is seen here when the experiments change from dry specimens

375 (-10°C) to relatively warm, floating, ones. In addition, the earlier work cited has shown that the dislocation density

376 increases with the salinity. Therefore, the calculated dislocation densities make sense physically and are generally

377 in line with expectations.

378 Specimens originating from two different ice sheets were tested. Table 4 shows that for a given set of conditions,

379 the elastic modulus of the specimens showed only small variations from one sheet to another. Compared with the

380 elastic modulus, the relative change in dislocation density was fairly large, which may be due to heterogeneity of

381 ice. A similar degree of change in dislocation density was also reported by Cole and Durell (2001) related to dry,

382 isothermal, ice specimens. As for the strength of the grain boundary relaxation, its value was taken as 2 ($\pm$1) $\times10^{-10}$

383 ^{10} Pa^{-1} for all specimens since variations in grain size among the ice specimens was small. Thus, here the main

384 quantity to be determined from the experimental results for studying anelastic strain response of the specimens

385 was the dislocation density. It was also found that for relatively high loading frequency (for example, 1 Hz used

386 here), the modeled strain behavior was dominated by the un-relaxed modulus E_0, not sensitive to the dislocation

387 density or the strength of grain boundary relaxation. However, for low-frequency (0.001 Hz) cyclic loading, the

388 modeled specimen deformation was very sensitive to the dislocation density.

389 The difference in the mechanical behavior between the floating and dry specimens has been mainly attributed to

390 temperature (Golden et al., 2007). Moreover, the specimens harvested from floating ice sheets lose brine once

391 removed from the sheet; warm ice in particular can lose a significant amount of brine which could significantly

392 alter the mechanical properties in subsequent experiments. In addition, some remaining brine (for example, some

393 of those in capillary brine channels) must freeze during the storage process of dry specimens; this may as well lead

394 to some difference in the macroscopic mechanical behavior (for example, in elastic modulus) of dry and floating

395 specimens (Marchenko and Lishman, 2017; Eicken, 1992; Jones et al., 2012; Gough et al., 2012). The methodology

396 developed in the present effort avoids such problems and is expected to produce more realistic mechanical behavior,

397 particularly when interest centers on behavior at relatively warm temperatures where brine drainage is extensive.

398 The analysis and modeling indicated that the physical mechanisms of deformation in both the warmer, floating

399 specimens and the colder dry specimens were essentially the same. Warmer saline ice had a smaller modulus due

400 to its higher liquid brine volume, which necessarily decreases the volume of the solid ice matrix (thereby reducing

401 the bulk elastic modulus) and there is a pronounced increase in effective dislocation density with increasing

402 temperature (Cole and Durell, 2001; Timco and Weeks, 2010; Cole, 2020). Thus, according to Eq. (10), although

403 the differences in ice temperature between the floating and dry experiments appear to result in an approximately

404 two-fold difference in the viscous component of strain, ε_v, this does not mean that the temperature will make the

405 viscous strain component of the floating ice only twice that of the dry ice. For example, the overall increase in

406 strain for specimen Floating-5ppt-1 is much higher (fifteen times more) than that for specimen Dry-5ppt-1. This

407 is mainly due to the aforementioned increase in effective dislocation density with increasing temperature (Cole

408 and Durell, 2001; Cole, 2020).

409 **6 Conclusions**

410 Equipment and methods were developed to conduct laboratory experiments to examine the mechanical properties

411 of floating saline ice specimens with a naturally occurring temperature gradient. In this initial effort, we examined

412 the strain response of floating saline ice under cyclic compressive stresses and conducted reference experiments

413 under dry, isothermal conditions. The experiments examined specimens having one of two nominal salinities (5

414 and 7 ppt), cyclic loading frequencies from 10^{-3} to 1 Hz were applied and two levels of cyclic stress were applied.

The experimental results compared favorably with the theoretical predictions obtained using a physically based constitutive model for saline ice. Given the limitations of the experiments program, the following conclusions can be drawn.

Equipment and methods:

1. Groups of unaligned, columnar grained saline ice specimens can be produced simultaneously in the laboratory using floating molds, and the presence of the molds has no observable effect on their microstructure.

2. The use of molds produced specimens that could be placed directly in the mechanical testing fixture, which for the case of floating ice experiments, provided a way to maintain a realistic temperature gradient during subsequent experimentation.

3. The experimental apparatus, which employed an electrohydraulic actuator and a saline water tank placed in a cold room, provided a way to apply in-plane loads to floating ice specimens and successfully produced monotonic and cyclic loading waveforms employed in more conventional systems.

Constitutive modeling:

4. The dislocation mechanics of the model employed in the analysis can reproduce well the strain response and energy dissipation of saline ice subjected to cyclic loading for floating ice or dry specimens, and for the observed ice salinities. The results show that the prediction errors of the energy density dissipation and the energy release rate are within $\approx 20\%$.

5. For either dry or floating specimens, the higher the salinity of ice, the lower the modulus (E_0) and the larger the dislocation density (ρ). In addition, E_0 is much higher and ρ is far smaller for the dry specimens than for the floating specimens, provided other experimental variables are consistent.

This work makes it clear that the mechanical behavior of floating specimens of saline ice can be examined in the laboratory under a reasonable approximation of in-situ conditions and with good efficiency. This capability opens the door to more sophisticated experimental work on saline ice under more realistic environmental conditions than previously possible.

Author contributions: AP, MW and DMC designed the study. MW and MP performed the experiments. MW, AP and DMC contributed to the interpretation of the results. MW, AP and DMC drafted the paper. All authors commented on the text.

Code and data availability: The code used for material modeling is written in MATLAB. Scripts used for analysis and more detailed information of the experimental results are available from the authors upon request.

Competing interests: The authors declare that they have no conflict of interest.

References

Blockley, E. W. and Peterson, K. A.: Improving Met Office seasonal predictions of Arctic sea ice using assimilation of CryoSat-2 thickness, The Cryosphere, 12, 3419–3438, https://doi.org/10.5194/tc-12-3419-2018, 2018.

Boe, J. L., Hall, A., and Qu X.: September sea-ice cover in the Arctic Ocean projected to vanish by 2100, Nat. Geosci., 2, 341–343, doi:10.1038/ngeo467, 2009.

Bond, P. E. and Langhorne, P. J.: Fatigue behavior of cantilever beams of saline ice, J. Cold Reg. Eng., 11, 99–112, https://doi.org/10.1061/(ASCE)0887-381X(1997)11:2(99), 1997.

Cheng, S., Tsarau, A., Evers, K. U., and Shen, H.: Floe size effect on gravity wave propagation through ice covers, J. Geophys. Res.-Oceans, 124, 320–334, https://doi.org/ 10.1029/2018JC014094, 2019.

Cole, D. M.: Reversed direct-stress testing of ice: Initial experimental results and analysis. Cold Reg. Sci. Technol., 18, 303–321, https://doi.org/10.1016/0165-232X(90)90027-T,1990.

Cole, D. M.: A model for the anelastic straining of saline ice subjected to cyclic loading, Philos. Mag. A, 72, 231–248, https://doi.org/10.1080/01418619508239592, 1995.

Cole, D. M.: On the physical basis for the creep of ice: the high temperature regime. J. Glaciol., 1–14. https://doi.org/10.1017/jog.2020.15, 2020.

Cole, D. M. and Dempsey, J. P.: Influence of scale on the constitutive behavior of sea ice, In: International Union of Theoretical and Applied Mechanics Symposium on Scaling Laws in Ice Mechanics and Ice Dynamics, pp. 251–264. Kluwer, Dordrecht, https://doi.org/10.1007/978-94-015-9735-7_22, 2001.

Cole, D. M. and Dempsey, J. P.: In situ sea ice experiments in McMurdo Sound: cyclic loading, fracture, and acoustic emissions, J. Cold Reg. Eng., 18, 155–174, https://doi.org/10.1061/(ASCE)0887-381X(2004)18:4(155), 2004.

Cole, D. M. and Durell, G. D.: The cyclic loading of saline ice, Philos. Mag. A, 72, 209–229, https://doi.org/10.1080/01418619508239591, 1995.

473 Cole, D. M. and Durell, G. D.: A dislocation-based analysis of strain history effects in ice, Philos. Mag. A, 81,
474   1849–1872, https://doi.org/10.1080/01418610108216640, 2001.

475 Cole, D. M., Johnson, R. A., and Durell, G. D.: Cyclic loading and creep response of aligned first-year sea ice, J.
476   Geophys. Res., 103, 21,751–21,758S, https://doi.org/10.1029/98JC01265, 1998.

477 Dempsey, J. P.: Research trends in ice mechanics, Int. J. Solids Struct., 37, 131–153,
478   https://doi.org/10.1016/S0020-7683(99)00084-0, 2000.

479 Dempsey, J. P., Adamson, R. M., and Mulmule. S. V.: Scale effects on the in-situ tensile strength and fracture of
480   ice, Part II: First-year sea ice at Resolute, N.W.T. Int. J. Fract., 95, 347–366,
481   https://doi.org/10.1023/A:1018650303385, 1999.

482 Dempsey, J. P., Cole, D. M., and Wang, S.: Tensile fracture of a single crack in first-year sea ice. Phil. Trans. R.
483   Soc. A, 376, https://doi.org/10.1098/rsta.2017.0346, 2018,

484 Eicken, H.: Salinity profiles of Antarctic sea ice: Field data and model results, J. Geophys. Res.-Oceans, 97,
485   15,545–15,557, https://doi.org/10.1029/92JC01588, 1992.

486 Feltham, D. L.: sea Ice rheology. Annu. Rev. Fluid Mech., 40, 91–112,
487   https://doi.org/10.1146/annurev.fluid.40.111406.102151, 2008.

488 Gagne, M. E., Gillett N. P., and Fyfe, J. C.: Observed and simulated changes in Antarctic sea ice extent over the
489   past 50 years, Geophys. Res. Lett., 42, 90–95, https://doi.org/10.1002/2014GL062231, 2015.

490 Golden, K. M., Eicken, H., Heaton, A. L., Miner, J., Pringle, D. J., and Zhu, J.: Thermal evolution of permeability
491   and microstructure in sea ice, Geophys. Res. Lett., 34, L16501, https://doi.org/10.1029/2007GL030447,
492   2007.

493 Gough, A. J., Mahoney, A. R., Langhorne, P. J., Williams, M. J. M., and Haskell, T. G.: Sea ice salinity and
494   structure: A winter time series of salinity and its distribution, J. Geophys. Res.-Oceans, 7, C03008,
495   https://doi.org/10.1029/2011JC007527, 2012.

496 Gow, A. J. Crystalline structure of urea ice sheets used in modeling experiments in the CRREL test basin. CRREL
497   report ; 84-24, https://hdl.handle.net/11681/9553, 1984.

498 Haskell, T. G., Robinson, W. H., and Langhorne, P. J.: Preliminary results from fatigue tests on in situ sea ice
499   beams, Cold Reg. Sci. Technol., 24, 167–176, https://doi.org/10.1016/0165-232X(95)00015-4, 1996.

500 Heijkoop, A. N., Nord, T. S., and Høyland, K. V.: Strain-controlled cyclic compression of sea ice. 24th IAHR
501   International Symposium on Ice Vladivostok, Russia, June 4 to 9, 2018.

502 Herman, A., Cheng, S., and Shen, H. H.: Wave energy attenuation in fields of colliding ice floes – Part 1: Discrete-
503   element modelling of dissipation due to ice–water drag, The Cryosphere, 13, 2887–2900,
504   https://doi.org/10.5194/tc-13-2887-2019, 2019a.

505 Herman, A., Cheng S., and Shen, H. H.: Wave energy attenuation in fields of colliding ice floes – Part 2: A
506   laboratory case study, The Cryosphere, 13, 2901–2914, https://doi.org/10.5194/tc-13-2901-2019, 2019b.

507 Iliescu, D. and Schulson, E. M.: Brittle compressive failure of ice: monotonic versus cyclic loading, Acta Mater.,
508   50, 2163–2172, https://doi.org/10.1016/S1359-6454(02)00060-5, 2002.

509 Iliescu, D., Murdza, A., Schulson, E. M., and Renshaw, C. E.: Strengthening ice through cyclic loading, J. Glaciol.,
510   63, 663–669, https://doi.org/10.1017/jog.2017.32, 2017.

511 Jones, K. A., Ingham, M., and Eicken, H. Modeling the anisotropic brine microstructure in first‐year arctic sea
512   ice, J. Geophys. Res.-Oceans, 117, C02005, doi:10.1029/2011JC007607, 2012.

513 Kartashkin, B. D.: Experimental studies of the physico-mechanical properties of ice, Tsentra'nyy
514   Aerogidrodinamicheskiy Institut, 1947

515 Kern, S., Lavergne, T., Notz, D., Pedersen, L. T., Tonboe, R. T., Saldo, R., and Sørensen, A. M. D.: Satellite passive
516   microwave sea-ice concentration data set intercomparison: closed ice and ship-based observations, The
517   Cryosphere, 13, 3261–3307, https://doi.org/10.5194/tc-13-3261-2019, 2019.

518 Langway, C. C.: Ice fabrics and the universal stage, Report # 62, CRREL, 1958.

519 Langhorne, P. J., Squire, V. A., Fox, C., and Haskell, T. G.: Break-up of sea ice by ocean waves, Ann. Glaciol., 27,
520   438–442, https://doi.org/10.3189/S0260305500017869, 1998.

521 Langhorne, P. J., Hughes, K. G., Gough, A. J., Smith, I. J., Williams, M. J. M., Robinson, N. J., Stevens, C. L.,
522   Rack, W., Price, D., Leonard, G. H., Mahoney, A. R., Haas, C., and Haskell, T. G.: Observed platelet ice
523   distributions in Antarctic sea ice: An index for ocean-ice shelf heat flux, Geophys. Res. Lett., 42, 5442–
524   5451, https://doi.org/10.1002/2015GL064508, 2015.

525 Leclair, E. S., Schapery, R. A., and Dempsey, J. P.: A broad-spectrum constitutive modeling technique applied to
526   saline ice, Int. J. Fract., 97, 209–226, https://doi.org/10.1023/A:1018358923672, 1999.

527 Li, J., Kohout, A. L., and Shen, H. H.: Comparison of wave propagation through ice covers in calm and storm
528   conditions, Geophys. Res. Lett., 42, 5935–5941, https://doi.org/10.1002/2015GL064715, 2015.

529 Li, Z., Riska, K.: Preliminary study of physical and mechanical properties of model ice. Technical Report M-212.
530   Helsinki University of Technology, 1996.

531 Liu, Y., Dai, F., Dong, L., Xu N., and Feng, P.: Experimental investigation on the fatigue mechanical properties of
532   intermittently jointed rock models under cyclic uniaxial compression with different loading parameters,
533   Rock Mech. Rock Eng., 51, 47–68, https://doi.org/10.1007/s00603-017-1327-7, 2018.

534 Liu, Y., Dai, F., Fan, P., Xu, N., and Dong, L.: Experimental investigation of the influence of joint geometric
535   configurations on the mechanical properties of intermittent jointed rock models under cyclic uniaxial
536   compression, Rock Mech. Rock Eng., 50, 453–1471, https://doi.org/10.1007/s00603-017-1190-6, 2017

537 Lu, W. and Løset, S.: Parallel channels' fracturing mechanism during ice management operations. Part II:
538   Experiment, Cold Reg. Sci. Technol., 156, 117–133, https://doi.org/10.1016/j.coldregions.2018.07.011,
539   2018.

540 Lu, W., Lubbad, R., Shestov, A., and Løset, S.: Parallel channels' fracturing mechanism during ice management
541   operations, Part I: Theory. Cold Reg. Sci. Technol., 156, 102–116,
542   https://doi.org/10.1016/j.coldregions.2018.07.010, 2018.

543 Marchenko, A. and Lishman, B.: The influence of closed brine pockets and permeable brine channels on the
544   thermo-elastic properties of saline ice. Phil. Trans. R. Soc. A, 375, 20150351,
545   http://dx.doi.org/10.1098/rsta.2015.0351, 2017.

546 Mellor, M. and Cole, D.: Cyclic loading and fatigue in ice. Cold Reg. Sci. Technol., 4, 41-53,
547   https://doi.org/10.1016/0165-232X(81)90029-X, 1981.

548 Murdza, A., Schulson, E. M., and Renshaw, C. E.: Hysteretic behavior of freshwater ice under cyclic loading: A
549   preliminary results. 24th IAHR International Symposium on Ice. Vladivostok, 185–192, 2018.

550 Murdza, A., Schulson, E. M., and Renshaw, C. E.: The effect of cyclic loading on the flexural strength of columnar
551   freshwater ice. In the Proceedings of the 25th International Conference on Port and Ocean Engineering
552   under Arctic Conditions (POAC'19). Electronic publication, 2019.

553   O'Connor DT, West BA, Haehnel RB, Asenath-Smith E, Cole D. A viscoelastic integral formulation and numerical
554   implementation of an isotropic constitutive model of saline ice, Cold Reg. Sci. Technol., 171, 102983,
555   https://doi.org/10.1016/j.coldregions.2019.102983, 2020.

556   Polojärvi, A., Tuhkuri, J., and Pustogvar, A. DEM simulations of direct shear box experiments of ice rubble: Force
557   chains and peak loads, Cold Reg. Sci. Technol., 116, 12–23,
558   https://doi.org/10.1016/j.coldregions.2015.03.011, 2015.

559   Ranta, J., Polojärvi, A., and Tuhkuri, J. The statistical analysis of peak ice loads in a simulated ice-structure
560   interaction process, Cold Reg. Sci. Technol., 133, 46–55,
561   https://doi.org/10.1016/j.coldregions.2016.10.002, 2017.

562   Ranta, J., Polojärvi, A., and Tuhkuri, J.: Ice loads on inclined marine structures - Virtual experiments on ice failure
563   process evolution, Mar. Struct., 57, 72–86, https://doi.org/10.1016/j.marstruc.2017.09.004, 2018a.

564   Ranta, J., Polojärvi, A., and Tuhkuri, J.: Limit mechanisms for ice loads on inclined structures: Buckling, Cold
565   Reg. Sci. Technol., 147, 34–44, https://doi.org/10.1016/j.coldregions.2017.12.009, 2018b.

566   Reistad, M., Breivik, Ø., Haakenstad, H., Aarnes, O. J., Furevik, B. R., and Bidlot, J. R.: A high-resolution hindcast
567   of wind and waves for the North Sea, the Norwegian Sea, and the Barents Sea, J. Geophys. Res., 116,
568   C05019, https://doi.org/10.1029/2010JC006402, 2011.

569   Ridley, J. K. and Blockley, E. W.: Brief communication: Solar radiation management not as effective as CO_2
570   mitigation for Arctic sea ice loss in hitting the 1.5 and 2 °C COP climate targets, The Cryosphere, 12,
571   3355–3360, https://doi.org/10.5194/tc-12-3355-2018, 2018.

572   Schulson, E. M. and Duval, P.: Creep and fracture of ice, Cambridge University Press, Cambridge, 2009.

573   Serreze, M. C. and Stroeve, J.: Arctic sea ice trends, variability and implications for seasonal ice forecasting, Phil.
574   Trans. R. Soc. A, 373, 20140159, http://dx.doi.org/10.1098/rsta.2014.0159, 2015.

575   Smith, I. J., Gough, A. J., Langhorne, P. J., Mahoney, A. R., Leonard, G. H., Van Hale, R., Jendersie, S., and
576   Haskellf, T. G.: First-year land-fast Antarctic sea ice as an archive of ice shelf meltwater fluxes, Cold
577   Reg. Sci. Technol., 113, 63–70, https://doi.org/10.1016/j.coldregions.2015.01.007, 2015.

578   Tabata, T. and Nohguchi, Y.: Failure of sea ice by repeated compression, In: Tryde P. (eds) Physics and Mechanics
579   of Ice, International Union of Theoretical and Applied Mechanics, Springer, Berlin, Heidelberg, 351–362,
580   https://doi.org/10.1007/978-3-642-81434-1_25, 1980.

581   Timco, G. W. and Weeks, W. F.: A review of the engineering properties of sea ice, Cold Reg. Sci. Technol., 60,
582   107–129, https://doi.org/10.1016/j.coldregions.2009.10.003, 2010.

583   Tuhkuri, J. and Polojärvi, A.: A review of discrete element simulation of ice-structure interaction, Phil. Trans. R.
584   Soc. A, 376, 20170335, http://dx.doi.org/10.1098/rsta.2017.0335, 2018.

585   Vincent, M. R. and Dempsey, J. P.: Servo-hydraulic pin loading device (HPLD) for in situ ice testing, J. Cold Reg.
586   Eng., 13, 21–36, https://doi.org/10.1061/(ASCE)0887-381X(1999)13:1(21), 1999.

587   Voermans, J. J., Babanin, A. V., Thomson, J., Smith, M. M., and Shen, H. H.: Wave attenuation by sea ice
588   turbulence, Geophys. Res. Lett., 46, 6796–6803, https://doi.org/10.1029/2019GL082945, 2019.

589   Weber, L. J. and Nixon, W. A.: Hysteretic behavior in ice under fatigue loading. Proceedings of the 15th
590   International Conference on Offshore Mechanics and Arctic Engineering. 75–82, 1996.

591 Wongpan, P., Hughes, K. G., Langhorne, P. J., and Smith, I. J.: Brine Convection, temperature fluctuations, and
592   permeability in winter Antarctic land-fast sea ice, 123, 216–230, https://doi.org/10.1002/2017JC012999,
593   2018.

594 Zijlema, M., Vledder, G. Ph. van, and Holthuijsen, L. H.: Bottom friction and wind drag for wave models, Coast.
595   Eng., 65, 19–26, https://doi.org/10.1016/j.coastaleng.2012.03.002, 2012.

596
597

598 **Table 1 The test matrix of this experimental campaign. The campaign included two test types, two ice**
599 **salinities, six periods and two test-type-dependent load levels. For each case, two specimens harvested from**
600 **two ice sheets were tested.**

Case	Specimen no.	Ice salinity (ppt)	Dry/Floating	Average ice temperature (°C)	Period (s)	Cyclic compressive Stresses (MPa)
I	Dry-5ppt-1, Dry-5ppt-2	5	Dry	-10	1, 5, 10, 100, 500, 1000	0.08–0.25
II	Dry-7ppt-1, Dry-7ppt-2	7	Dry	-10	1, 5, 10, 100, 500, 1000	0.08–0.25
III	Floating-5ppt-1, Floating-5ppt-2	5	Floating	-2.5	1, 5, 10, 100, 500, 1000	0.04–0.12
IV	Floating-7ppt-1, Floating-7ppt-2	7	Floating	-2.5	1, 5, 10, 100, 500, 1000	0.04–0.12

601

602 **Table 2 The energy density ($J \cdot m^{-3}$) dissipated in a typical loading-unloading cycle of each experiment.**

Specimen no.	Frequency (Hz)				
	0.001	0.002	0.01	0.1	0.2
Dry-5ppt-1	8.83	5.44	2.01	0.67	0.71
Dry-5ppt-2	5.36	2.93	1.57	0.54	0.36
Dry-7ppt-1	14.4	7.16	2.87	0.91	0.66
Dry-7ppt-2	20.8	14.0	7.80	2.49	2.05
Floating-5ppt-1	25.0	15.4	4.78	0.85	0.63
Floating-5ppt-2	28.4	16.2	4.79	0.91	0.54
Floating-7ppt-1	151	67.7	20.2	3.85	2.52
Floating-7ppt-2	63.6	38.3	11.7	2.40	1.63

603

604 **Table 3 The energy dissipation rate (%) in a typical loading-unloading cycle of each experiment.**

Specimen no.	Frequency (Hz)				
	0.001	0.002	0.01	0.1	0.2
Dry-5ppt-1	48.3	40.2	22.0	9.86	9.93
Dry-5ppt-2	35.4	22.7	17.6	8.68	5.50
Dry-7ppt-1	55.6	37.3	21.6	11.0	8.60
Dry-7ppt-2	55.7	44.7	32.3	16.0	14.3
Floating-5ppt-1	89.6	76.1	44.2	15.5	11.8
Floating-5ppt-2	87.7	69.8	39.4	17.4	11.3
Floating-7ppt-1	98.3	91.7	70.5	32.0	25.1
Floating-7ppt-2	88.1	76.0	56.4	26.3	20.2

Table 4. Values of the model parameters calibrated for simulating the strain response of the ice specimens (in Section 5, these values are discussed and compared to those reported in references).

Specimen no.	Elastic modulus E_0 (GPa)	Dislocation density ρ (m^{-2})	Strength of dislocation relaxation δD^d (Pa^{-1})	Strength of grain boundary δD^{gb} (Pa^{-1})
Dry-5ppt-1	6.0	7.53×10^8	7×10^{-10}	1×10^{-10}
Dry-5ppt-2	5.6	4.31×10^8	4×10^{-10}	1×10^{-10}
Dry-7ppt-1	4.0	1.18×10^9	1.1×10^{-9}	1×10^{-10}
Dry-7ppt-2	4.0	1.83×10^9	1.7×10^{-9}	3×10^{-10}
Floating-5ppt-1	2.0	5.92×10^9	5.5×10^{-9}	3×10^{-10}
Floating-5ppt-2	1.9	6.46×10^9	6×10^{-9}	1×10^{-10}
Floating-7ppt-1	1.9	2.58×10^{10}	2.4×10^{-8}	3×10^{-10}
Floating-7ppt-2	1.7	1.40×10^{10}	1.3×10^{-8}	2×10^{-10}

Table 5. Modeling results of the strain energy density (J·m^{-3}) dissipated per loading-unloading cycle (the values given in parentheses are error percentages of model predictions relative to experimental results).

Specimen no.	Frequency				
	0.001 Hz	0.002 Hz	0.01 Hz	0.1 Hz	0.2 Hz
Dry-5ppt-1	9.12 (7%)	5.16 (9%)	1.74 (-10%)	0.69 (-9%)	0.68 (-21%)
Dry-5ppt-2	5.22 (-3%)	3.10 (6%)	1.15 (-27%)	0.55 (2%)	0.33 (-8%)
Dry-7ppt-1	15.1 (5%)	8.76 (22%)	2.65 (-8%)	0.86 (-5%)	0.79 (20%)
Dry-7ppt-2	21.9 (-1%)	12.5 (-4%)	6.44 (-9%)	2.00 (-22%)	1.97 (12%)
Floating-5ppt-1	27.0 (8%)	14.9 (-3%)	4.05 (-15%)	0.91 (7%)	0.73 (16%)
Floating-5ppt-2	30.3 (3%)	16.8 (1%)	4.58 (-6%)	0.89 (-17%)	0.61 (-8%)
Floating-7ppt-1	125 (-17%)	68.5 (1%)	18.6 (-8%)	3.79 (-2%)	2.58 (2%)
Floating-7ppt-2	65.4 (-17%)	36.4 (-4%)	10.0 (-21%)	2.18 (10%)	1.73 (13%)

615

616 **Table 6. Modeling results of the strain energy dissipation rate (%) per loading-unloading cycle (the values given in parentheses are error percentages of model predictions relative to experimental results).**

Specimen no.	Frequency				
	0.001 Hz	0.002 Hz	0.01 Hz	0.1 Hz	0.2 Hz
Dry-5ppt-1	49.2 (4%)	36.7 (-1%)	18.5 (-13%)	9.43 (-12%)	9.81 (-16%)
Dry-5ppt-2	37.4 (16%)	25.9 (14%)	13.9 (-21%)	7.5 (-5%)	5.70 (12%)
Dry-7ppt-1	53.1 (-1%)	41.3 (-2%)	20.2 (10%)	8.99 (-18%)	8.50 (12%)
Dry-7ppt-2	51.3 (-1%)	38.9 (-2%)	25.7 (10%)	12.6 (-18%)	13.9 (12%)
Floating-5ppt-1	87.8 (-5%)	77.1 (-4%)	40.0 (-15%)	16.0 (3%)	14.0 (3%)
Floating-5ppt-2	91.1 (-1%)	82.0 (6%)	45.1 (-4%)	17.6 (9%)	13.4 (26%)
Floating-7ppt-1	86.4 (-1%)	77.4 (-3%)	59.9 (-10%)	34.0 (13%)	28.2 (17%)
Floating-7ppt-2	94.5 (-1%)	88.3 (-3%)	52.9 (-10%)	23.8 (13%)	20.5 (17%)

617

618

Power plugs for
the heating cables

The hose for alleviating water
pressure during ice growth

Plastic molds

The plywood tank covered
with thermo-insulating foams
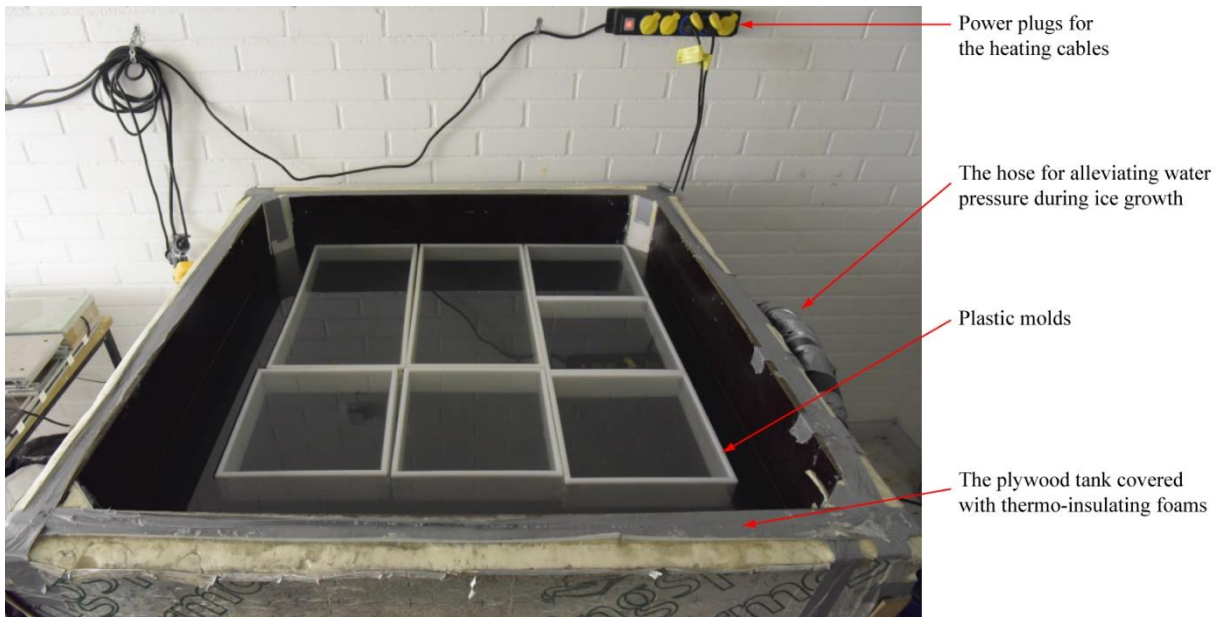
619   **Figure 1. The tank made of plywood for growing ice specimens.**

620

621   (a)   (b)

622 **Figure 2. Equipment used in the (a) dry and (b) floating ice experiments. One of the plastic molds used when**

623 **growing ice is shown in (b). The thin ice cover of the basin, seen in (b), was broken before performing the**

624 **experiments.**
625

626
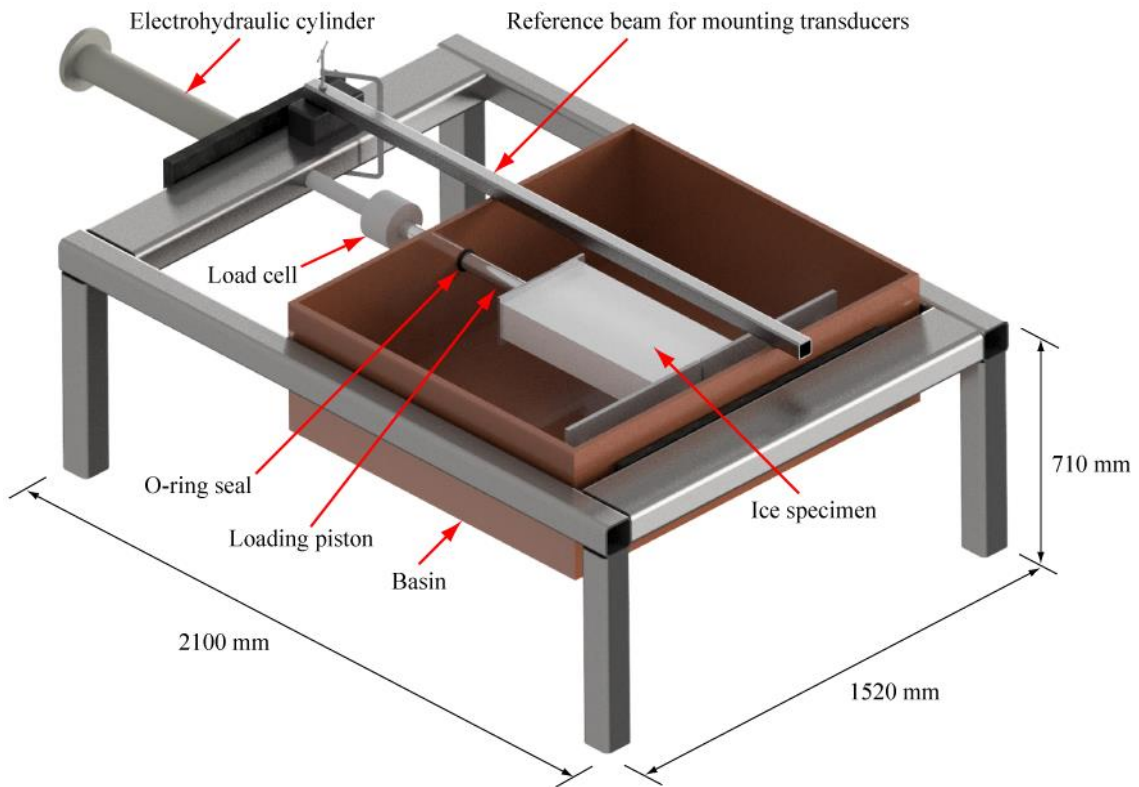
Figure 3. A sketch of the test rig used in the experiments. The inner dimensions of the basin are 1320 mm ×
1280 mm × 400 mm.

629

(a)　　　　　　　　　　　　　　　(b)
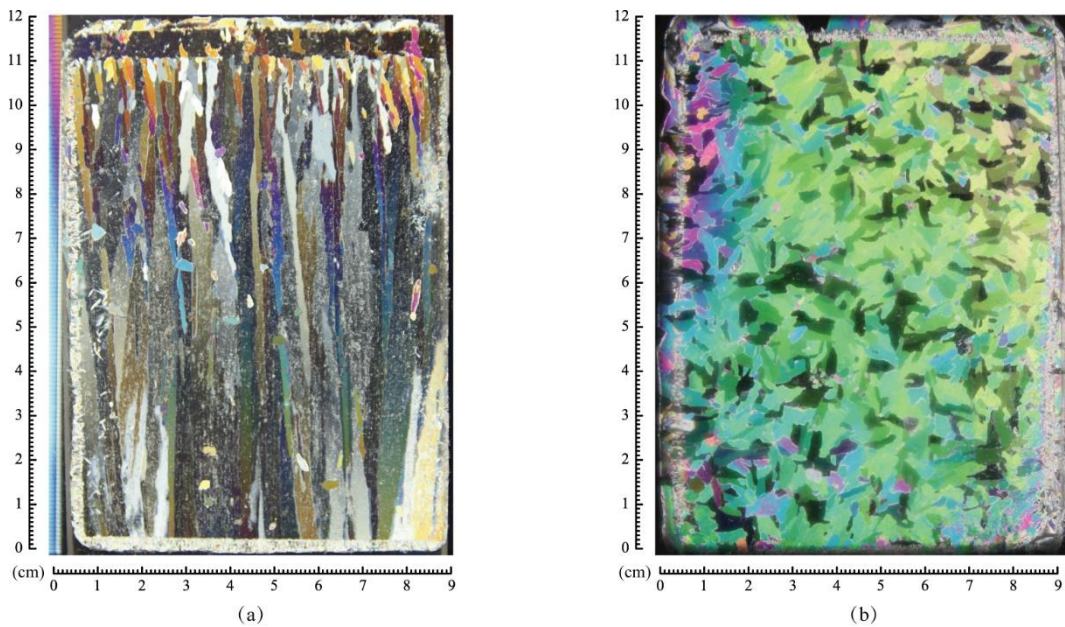
Figure 4. One set of thin sections of the ice (salinity: 5 ppt) grown in this experimental campaign: (a) vertical;
(b) horizontal.

633

634
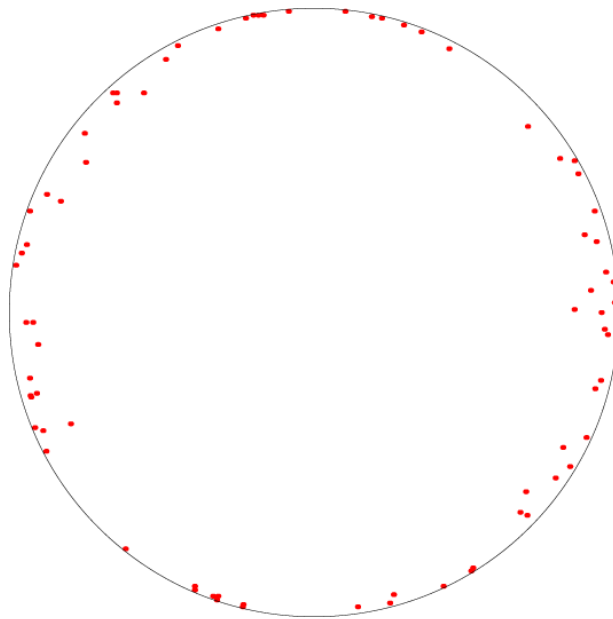
Figure 5. A typical Schmidt equal area net pole projection drawn on the basis of grain orientations.

635

636
637

(a)　　　　　　　　　　　　　　(b)

638
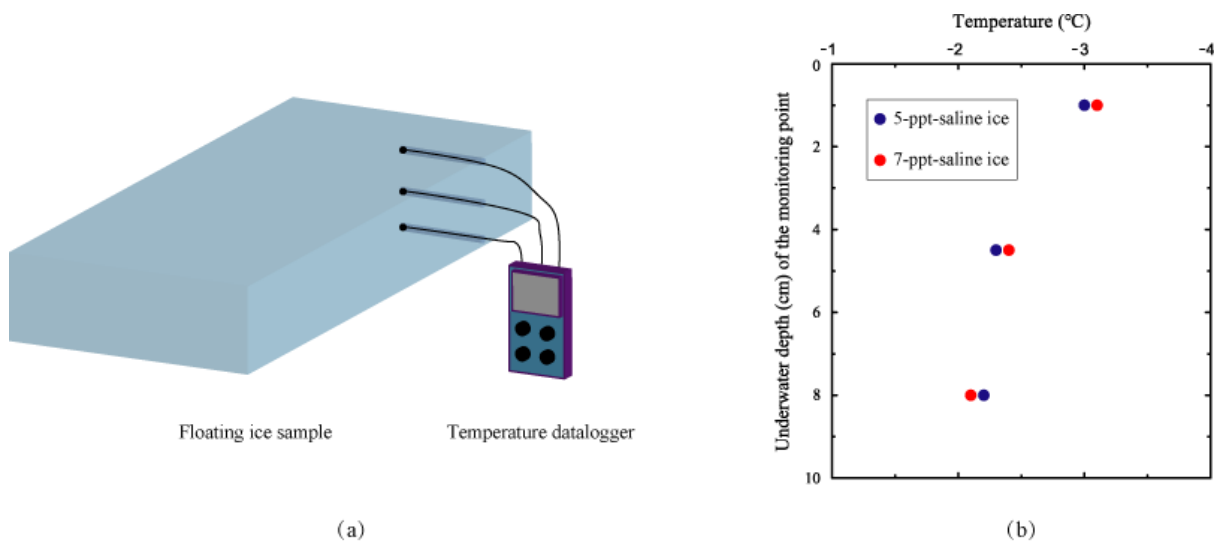
Figure 6. Monitoring of the through-thickness thermal gradient of floating ice: (a) a schematic diagram of the arrangement of the temperature probes and (b) the measured through-thickness thermal gradient inside two floating ice specimens.

639

640

641

642

(a)　　　　　　　　　　(b)
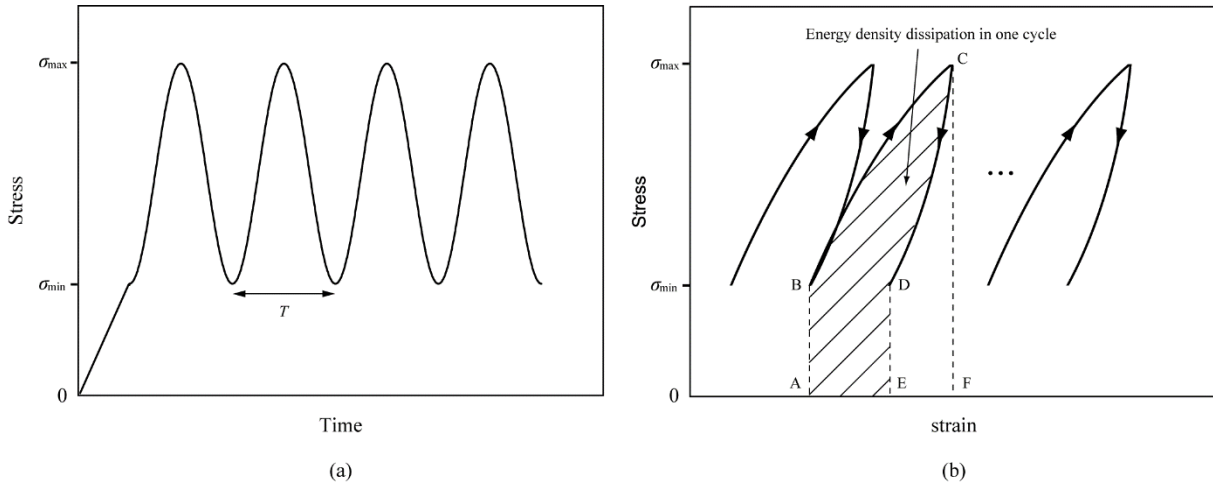
643

644 **Figure 7. Schematic diagrams of the cyclic loads: (a) the inputted stress waveform, and (b) the method for calculating the energy density dissipated in one loading cycle (in other words, region ABCDE).**

645
646
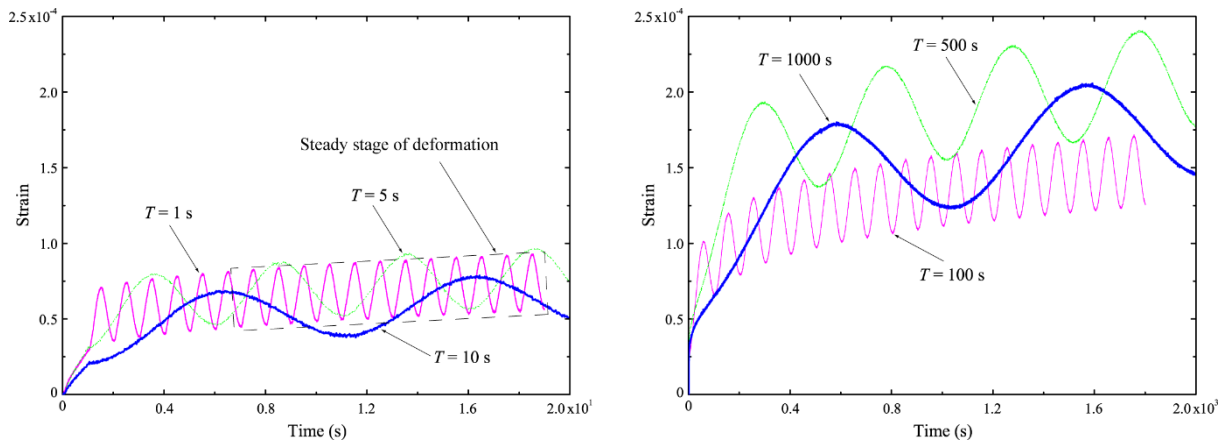
647 **Figure 8. Strain-time curves of specimen Dry-5ppt-1 tested with stresses varying from 0.08 to 0.25 MPa and**
648 **with the temperature of -10°C.**
649

650
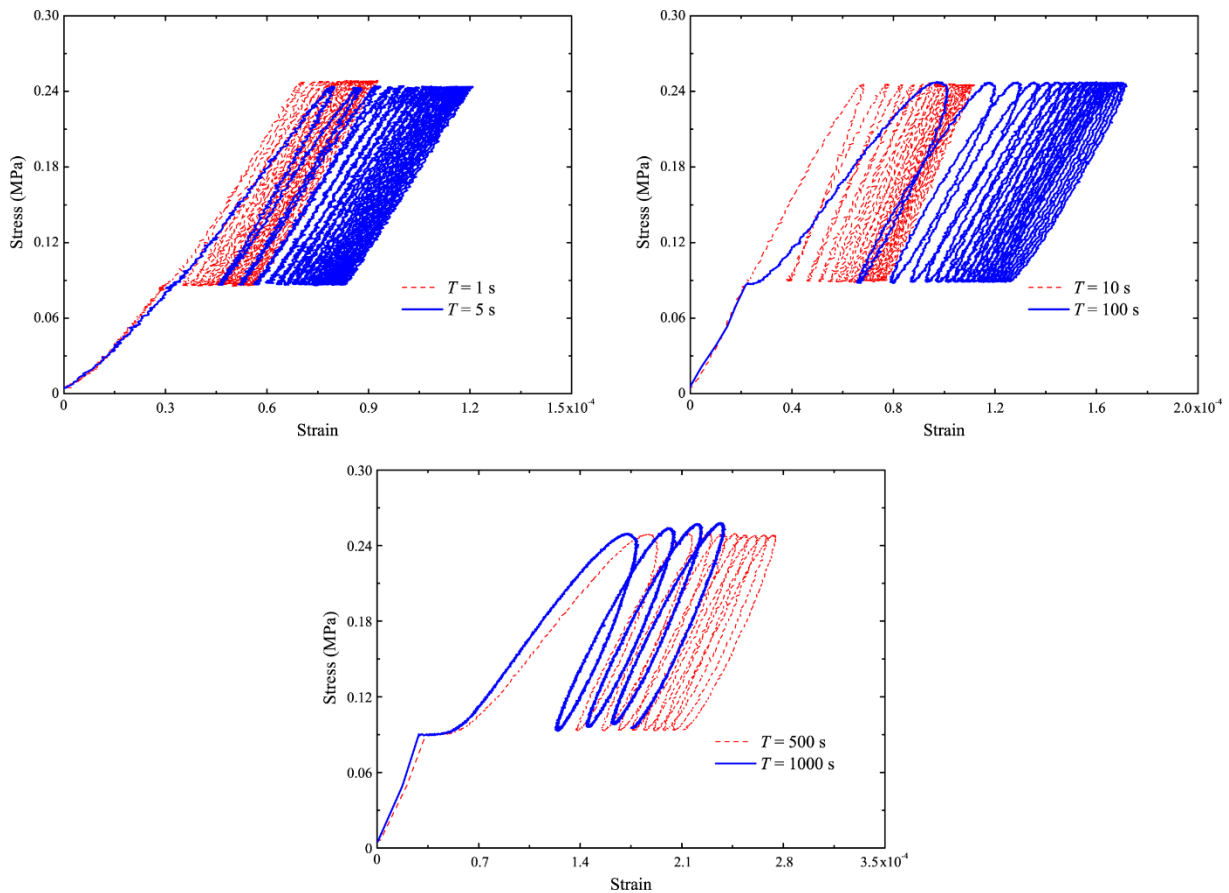
651
652
Figure 9. Stress-strain curves of specimen Dry-5ppt-1 tested with stresses varying from 0.08 to 0.25 MPa and with the temperature of -10°C.

653
654

(a)   (b)
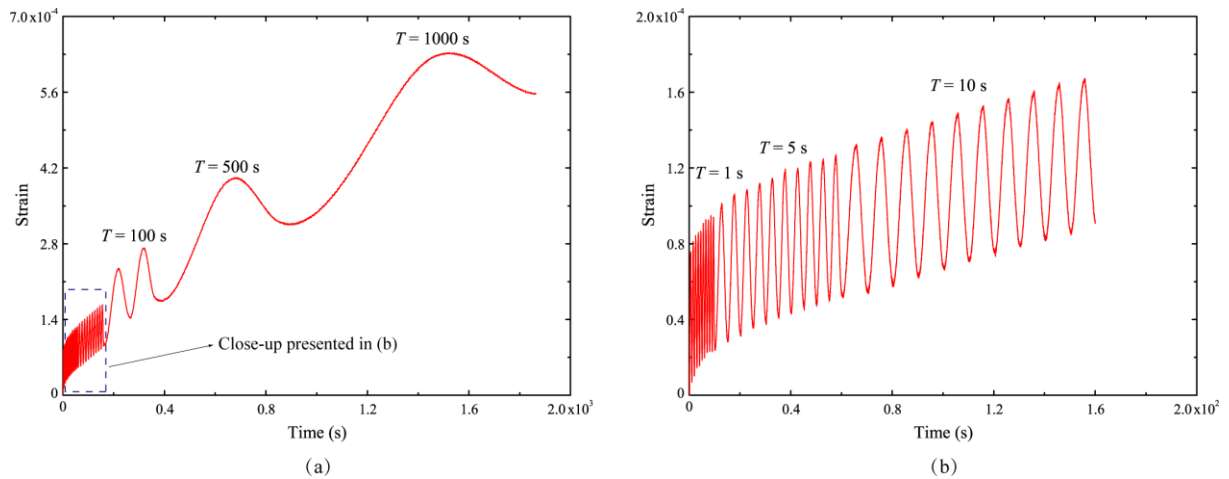
655
656
657
658
Figure 10. Strain response of specimen Floating-5ppt-1 tested with stresses varying from 0.04 to 0.12 MPa and with the average temperature of -2.5°C: (a) shows the response for all periods, T, of cyclic loading, while (b) presents a close-up showing the cycles for $T = 1, 5$ and 10 s.

659

(a)

(b)
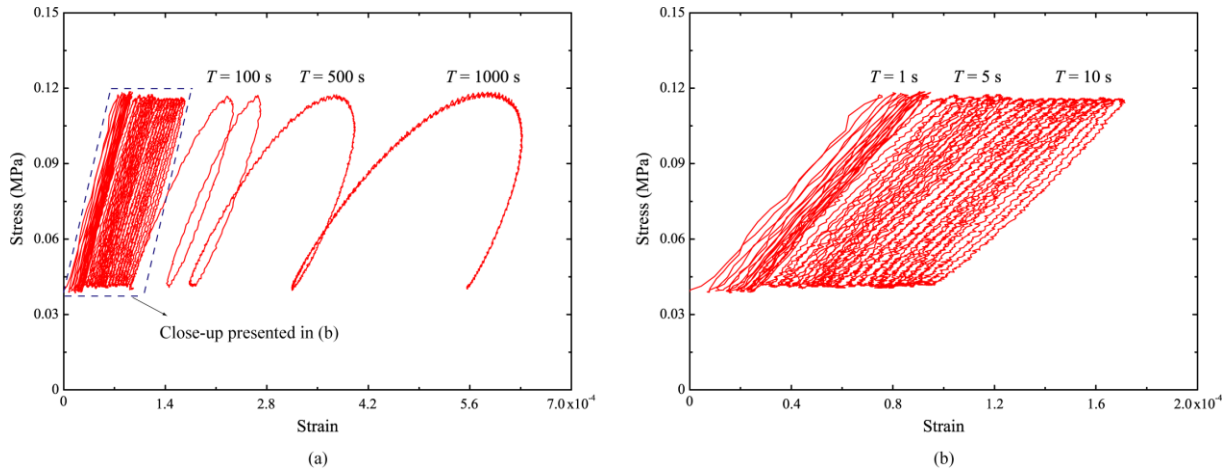
660

661

662

Figure 11. Stress-strain plots of specimen Floating-5ppt-1 tested with stresses varying from 0.04 to 0.12 MPa and with the average temperature of -2.5°C: (a) shows the response for all periods, *T*, of cyclic loading, while (b) presents a close-up showing the cycles for *T* = 1, 5 and 10 s.

663
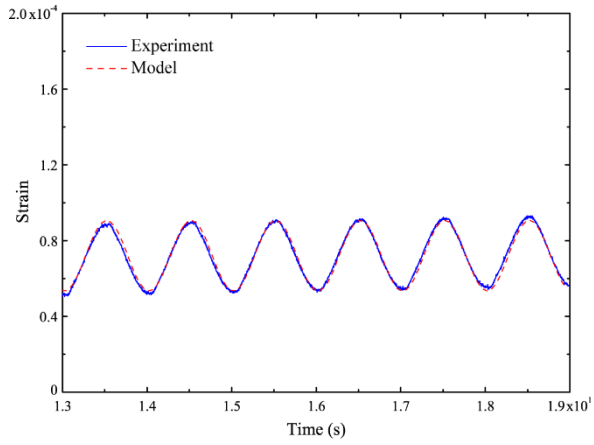
(a) *T* = 1 s
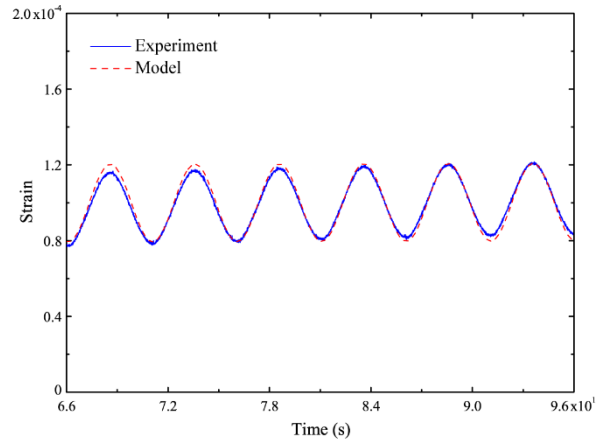
(b) *T* = 5 s
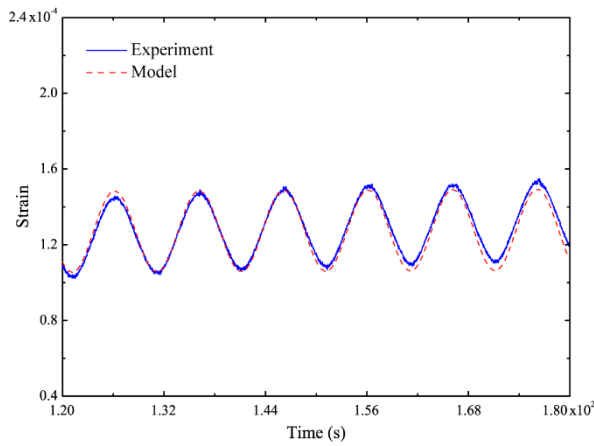
(c) *T* = 10 s
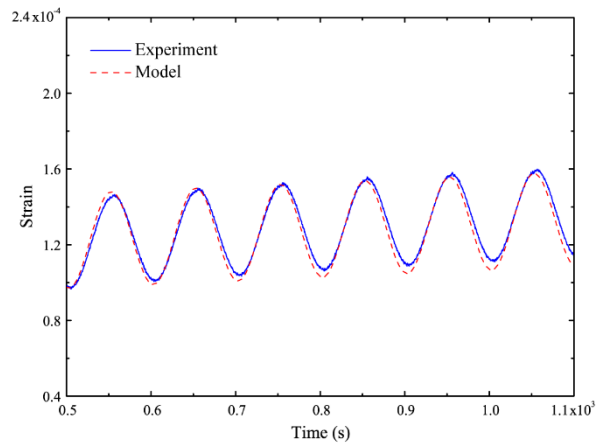
(d) *T* = 100 s
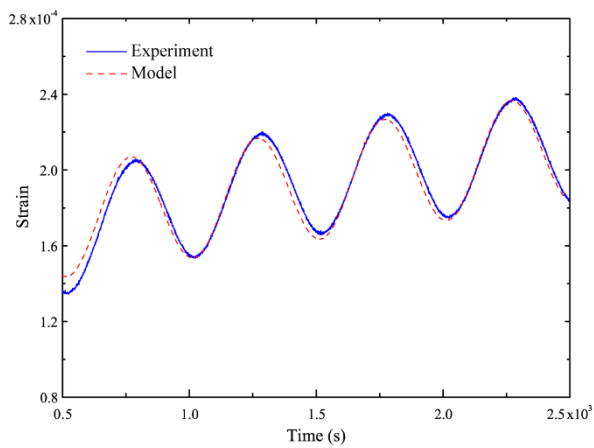
(e) *T* = 500 s
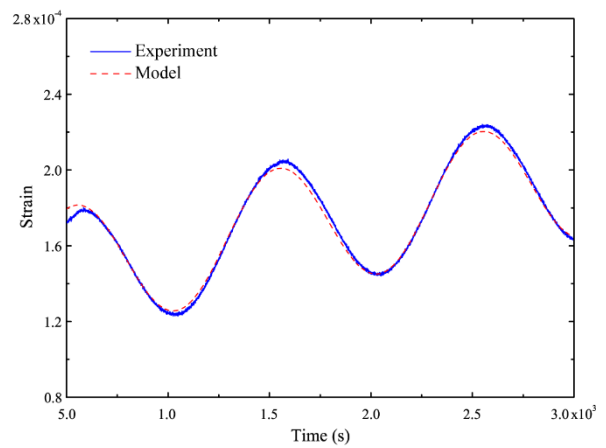
(f) *T* = 1000 s

664
665
666

Figure 12. Comparison between the experimentally measured strain-time curves (in the steady stage) and the results yielded by the physically based model for specimen Dry-5ppt-1 tested with stresses varying from 0.08 to 0.25 MPa and with the temperature of -10°C.
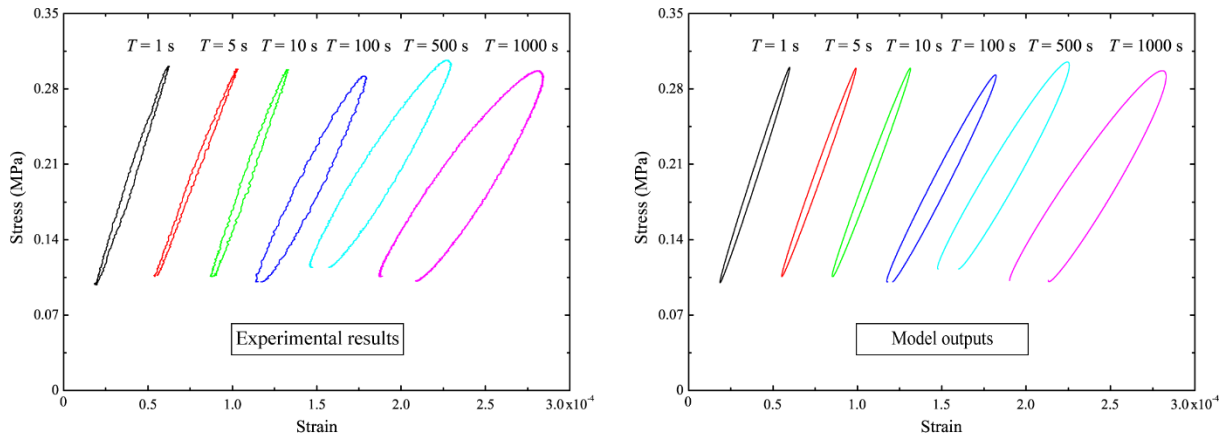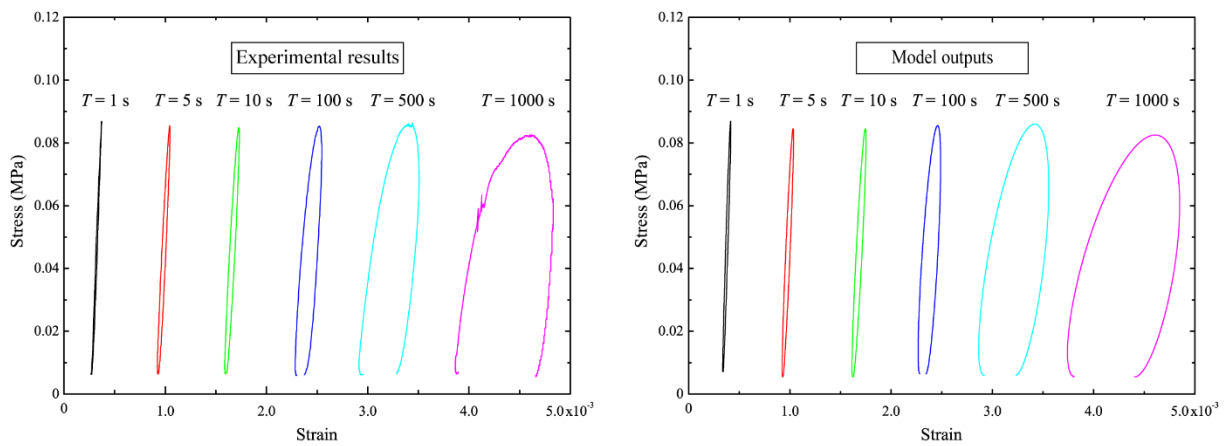
667

(a)

(b)
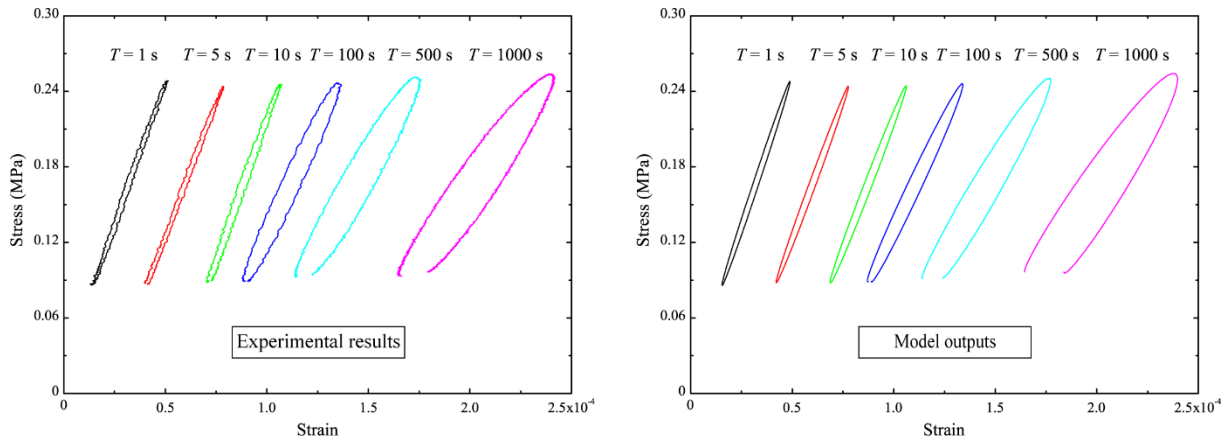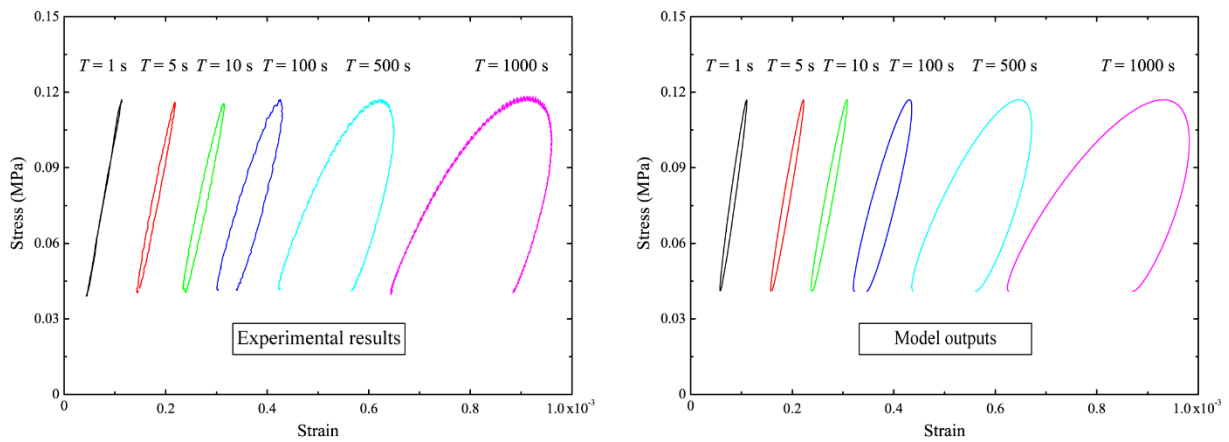
Figure 13. Comparison between the steady-state stress-strain hysteresis loop measured in the experiments and that outputted from the model for (a) specimen Dry-5ppt-1 with the temperature of -10°C and (b) specimen Floating-5ppt-1 with the average temperature of -2.5°C (note that, to compare the representative hysteresis loops in all the different-frequency experiments with those outputted by the model in a more concise and intuitive way, the pre-strains before the hysteresis loops drawn here are not equal to the experimental values).

Figure 14. Comparison between the steady-state stress-strain hysteresis loops measured in the experiments and those predicted by the dislocation-based model for (a) specimen Dry-5ppt-1 tested with stresses varying from 0.1 to 0.3 MPa and with the temperature of -10°C and (b) specimen Floating-5ppt-1 tested with stresses varying from 0.005 to 0.085 MPa and with the average temperature of -2.5°C (note that, to compare the representative hysteresis loops in all the different-frequency experiments with those outputted by the model in a more concise and intuitive way, the pre-strains before the hysteresis loops drawn here are not equal to the experimental values).